

Microscale modeling of effective mechanical and electrical properties of textiles

Alejandro Queiruga^{*,†} and Tarek Zohdi

Department of Mechanical Engineering, University of California, 6195 Etcheverry Hall, Berkeley, CA 94720-1740, USA

SUMMARY

A computational framework for assisting in the development of novel textiles is presented. Electronic textiles are key in the rapidly growing field of wearable electronics for both consumer and military uses. There are two main challenges to the modeling of electronic textiles: the discretization of the textile microstructure and the interaction between electromagnetic and mechanical fields. A director-based beam formulation with an assumed electrical current is used to discretize the fabric at the level of individual fibrils. The open-source package FEniCS was used to implement the finite element model. Contact integrals were added into the FEniCS framework so that multiphysics contact laws can be incorporated in the same framework, leveraging the code generation and automated differentiation capabilities of FEniCS to produce the tangents needed by the implicit solution method. The computational model is used to construct and determine the mechanical, thermal, and electrical properties of a representative volume elements of a plain woven textile. Dynamic relaxation to solve the mechanical fields and the electrical and thermal fields is solved statically for a given mechanical state. The simulated electrical responses are fit to a simplified Kirchhoff network model to determine effective resistances of the textile. Copyright © 2016 John Wiley & Sons, Ltd.

Received 9 February 2016; Revised 29 February 2016; Accepted 31 March 2016

1. INTRODUCTION

Textiles are one of the most common materials used and have widespread applications. They are characterized by their multiscale structure, wherein a single sheet of fabric is composed of a woven or knitted network of yarns, which are in turn composed of spun fibrils. Fabrics with novel mechanical, thermal, or electrical properties can be created by weaving different types of yarns made from different types of fibrils in various patterns. Designing new textile materials with exotic properties requires models with predictive capabilities for the multiphysics behavior. Circuits can be placed onto fabrics by embroidering conductive yarns onto standard fabrics [1, 2], using conductive paints [3, 4] or weaving conductive elements into the textile [5–8]. Besides conductive elements, more exotic materials have been incorporated into fabrics to add functionality, such as thermomechanical fibrils to create a textile actuator similar to that illustrated in Figure 1 as demonstrated in Haines [9] or piezoelectric yarns for force sensing [7] and energy harvesting [8].

The microstructure of textiles and heterogenous electrical materials makes accurate material computational modeling difficult. Homogenization of heterogenous polarizable materials using finite element models was performed in Kuznetsov [10]. However, the electrical properties of interwoven conducting and insulating elements examined in this work cannot be handled by homogenized continuum models. A review of methodologies for the numerical and experimental determination of textile behavior can be found in Wentrof [11]. Finite element simulations of textiles with the

^{*}Correspondence to: Alejandro Queiruga, Department of Mechanical Engineering, University of California, 6195 Etcheverry Hall, Berkeley, CA 94720-1740, USA.

[†]E-mail: afq@berkeley.edu

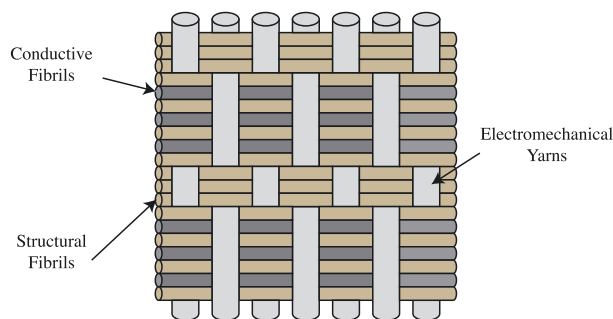


Figure 1. Example of a functionalized electronic textile with actuating yarn in the vertical direction and conductive and structural yarns in the horizontal direction. See [9] for a realized textile actuator of this design.

individual yarns discretized as solid meshes have been performed extensively [12, 13]. While the detail of such a discretization allows for many properties to be modeled, the inherent geometric structure of the fabric forces a large number of degrees of freedom for even a small piece of fabric. Multiscale models with meshed fibril microstructures were performed in [14]. An analytical solution of interlocking yarn beams is used as a constitutive model for a membrane finite element simulation in [15]. In [16], the fibril microstructure is meshed fully to produce a representative volume element of braided rope and used to produce effective properties for a beam model of the resulting yarn.

In order to preserve the global and local properties of the woven yarn structure, while still reducing the degrees of freedom required, lattice network models are employed, such as the finite element-oriented approach in Tan [17] and the analytical model in Leech [18]. Empirical damage laws and electromagnetic effects were incorporated into a network model in Zohdi [19–21]. Advanced summation techniques for network models designed for electronic textiles and applied to atomistic lattice models were developed in Beex [22].

The multi-chain digital element method represents individual fibrils as pin-jointed rod elements [23, 24]. The method is capable of static and sliding frictional contacts using a rod–rod contact geometry [25]. The digital elements were coupled with a vacuum bag model to simulate composite manufacturing in [26]. The method was used in [27] to perform a ballistic impact simulation on a fully discretized textile sheet with up to 19 fibrils per yarn in a 33 mm by 33 mm sheet with approximately 44 yarns in each direction. Fibrils are assembled into woven structures using a nonlinear beam description in Durville [28–30]. This method has been used in the study of nonwoven fabrics [28], biological tissue engineering [31], and knot forming [32], and the fatiguing of superconducting wires due to stresses arising from thermal and electrical loads [33, 34].

This work presents a model for electronic textiles based upon discretizing individual fibrils using a director-based beam finite element model. The beam formulation is expanded to include temperature and a carried electric current that are affected by contacts between beams, allowing the determination of electrical and thermal properties that are functions of strain state. Even utilizing a simplified beam-based model, the number of degrees of freedom required to simulate a large-scale textile with the complete discretization is intractable. Representative volume elements can be used to predict material properties quickly and efficiently to inform the design of new fabrics. This work focuses on fabrics without a matrix material, wherein individual fibrils are free to slide past one another, producing a plastic-type behavior at the macroscale. Plastic deformation and failure of the individual fibrils are not considered, but it is noted that the constitutive responses could be extended. The finite element model is implemented in the open-source package FEniCS [35] using extensions implemented by the authors to automatically generate the finite element code for integrals along beam contacts. A simple plain-woven textile unit cell consisting of conductive fibrils is studied, although the framework developed can handle arbitrary microstructures.

The mechanical and electromagnetic partial differential equations (PDEs) are described in Section 2, and the beam description with thermal and electromagnetic effects is described in Section 3. The treatment of contacts is described in Section 4. The variational forms of the

mechanical, electrical, and thermal problems are listed in Section 5. The analysis procedure is described in Section 6, and the details of the computer implementation and modifications to FEniCS are described in Section 7. The results of the computation are presented and discussed in Section 8. Finally, Section 9 contains concluding remarks.

2. FORMULATION

2.1. Material responses

The kinematic notation used is illustrated in Figure 2, with current configuration \mathbf{x} , reference configuration \mathbf{X} , ideal configuration ξ , and deformation gradient \mathbf{F} whose determinant is J (the Jacobian). The coordinate system ξ is defined for convenient description of the geometry of the long and thin fiber to allow this simplified deformation description. The reference (or natural, or unstrained) configuration, \mathbf{X}_0 , may differ from this ideal configuration; that is, a fiber may be naturally bent, but it is still easier to describe its deformation using the curvilinear system ξ . Basis vectors in the current configuration are denoted by \mathbf{e}_i , reference configuration basis vectors are denoted by \mathbf{E}_i , and ideal configuration basis vectors are denoted by $\hat{\mathbf{E}}_i$.

The temperature is represented by T , density by ρ , and right Cauchy–Green stretch tensor by $\mathbf{C} = \mathbf{F}^T \mathbf{F}$. While the studies presented in this work are static, a dynamic formulation is used to relax to static equilibrium. Thus, the electromagnetic responses are written using material frame invariants needed for correct treatment of dynamics. For a material moving with velocity \mathbf{v} , these are the conduction current density, $\mathcal{J} = \mathbf{j} - q\mathbf{v}$, with the spatial current density \mathbf{j} and charge density q , and the electromotive intensity, $\mathcal{E} = \mathbf{E} + \mathbf{v} \times \mathbf{B}$, with the spatial electric field \mathbf{E} and magnetic field \mathbf{B} . The reader is directed to Kovetz [36] and Steigmann [37] in particular for the theoretical basis for the coupling continuum mechanics and electromagnetism used throughout this work.

The material response is stated in terms of an internal strain energy density ψ that is in general a function of $\psi(\mathbf{C}, T, \mathbf{F}^T \mathcal{E}, \dots)$. This quantity does not include the energy stored in the electromagnetic fields themselves but would contain energy stored in material responses to electromagnetic fields, such as polarization or piezoelectric effects. Responses for ψ taking into account electromagnetic fields are possible but are neglected for the time being and will be considered in future work. A neo-Hookean hyperelastic constitutive law is used for the strain energy density,

$$\psi = \frac{\mu}{2} (\text{tr} \mathbf{C} - 3) - \mu \log J + \frac{\lambda}{2} (\log J)^2. \tag{1}$$

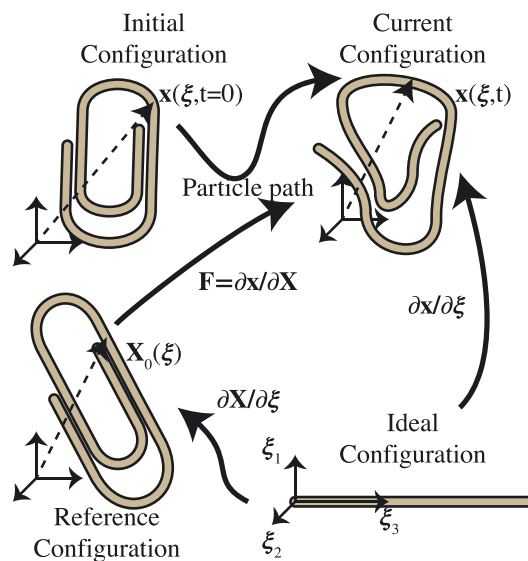


Figure 2. Configurations for describing finite deformation problems.

The strain energy function yields the first Piola–Kirchhoff stress tensor as the derivative with respect to the deformation gradient, $\mathbf{P} = \frac{\partial \psi}{\partial \mathbf{F}}$. The Lamé parameters μ and λ can be calculated from the Young's modulus E and Poisson ratio ν by $\mu = \frac{E}{2(1+\nu)}$ and $\lambda = \frac{E\nu}{(1+\nu)(1-2\nu)}$. Fourier's law couples the heat flux vector to the temperature gradient,

$$\mathbf{q} = -\mathbf{k}\nabla_x T, \quad (2)$$

where \mathbf{k} is the thermal conductivity tensor. Only scalar thermal conductivities are considered.

Conducting, non-polarizing beams that satisfy Ohm's law for a conductor are considered,

$$\mathcal{J} = \sigma \mathcal{E}, \quad (3)$$

where σ is the electrical conductivity tensor, which holds in the material's rest frame. As with the thermal conductivity, only isotropic materials are considered, so it will be treated as a scalar. Conducting materials exhibit Joule heating, which must also be phrased with the invariants,

$$r = \mathcal{J} \cdot \mathcal{E} = \mathcal{E} \cdot \sigma \mathcal{E}. \quad (4)$$

The Lorentz force is not considered for this work because of the absence of magnetic fields and accumulated free charges, so the electrical field will not effect the mechanical state.

2.2. Summary of field equations

The balance of linear momentum and the balance of energy PDEs are solved for the material deformation and temperature. The electromagnetic effects are treated by solving the lab frame electric potential V on the body, which is related to the lab frame electric field by $\mathbf{E} = -\nabla_x V$. In the static case, only charge conservation, $\nabla \cdot \mathcal{J} = \frac{\partial}{\partial t} q + \nabla \cdot q\mathbf{v}$ yielding $\nabla \cdot \mathcal{J} = 0$, needs to be solved. Thus, the Laplacian for the potential scaled by conductivity tensor needs to be solve,

$$\nabla_x \cdot \sigma \nabla_x V = 0. \quad (5)$$

The equations are pushed back into the reference and ideal configurations for solution, where subscript naught denotes a value evaluated in the material reference configuration, while a subscript ξ denotes a value evaluated in the ideal configuration. The three coupled PDEs derived can be summarized by their reference configuration forms,

$$\rho_0 \ddot{\mathbf{x}} = \nabla_X \cdot \frac{\partial \psi}{\partial \mathbf{F}} + J \mathbf{f}, \quad (6)$$

$$0 = \nabla_X \cdot \mathbf{k}_0 \nabla_X T + J (\mathcal{J} \cdot \mathcal{E} + r), \quad (7)$$

$$0 = \nabla_X \cdot \sigma_0 \nabla_X V. \quad (8)$$

where \mathbf{f} and r are force and heat generation densities that are not electromagnetic in nature. Boundary conditions for contacts are described in Section 4.2. The three aforementioned equations can be solved fully coupled dynamically but are separated for the material property prediction setup, wherein the electric potential follows the mechanical state and the temperature depends on both the electric field and mechanical state.

3. CURRENT-CARRYING BEAM

A kinematic director-based beam model is used, wherein in a one-dimensional finite element basis, it is used along the axis and an ansatz is used along the cross section to construct the displacement field using two vector directors, as diagrammed in Figure 3. For a discussion of director-based theories, see Rubin [38]. Thermal and electromagnetic fields are incorporated into the beam formulation with additional constant ansätze for the temperature and electric current along the cross section.

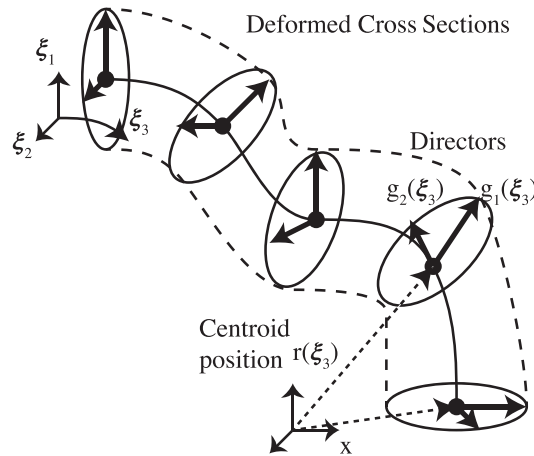


Figure 3. Director-based beam formulation.

3.1. Director-based beam model

The ideal configuration of the beam has coordinates ξ_1, ξ_2 along the cross section and ξ_3 along the axis, with the curvilinear orthonormal basis vectors $\hat{\mathbf{E}}_1, \hat{\mathbf{E}}_2$, and $\hat{\mathbf{E}}_3$, respectively. Let $\mathbf{r}(\xi_3)$ denote the position of the centroid of a given cross section of the fiber, and $\mathbf{g}_1(\xi_3)$ and $\mathbf{g}_2(\xi_3)$ denote the directors of the cross section in the directions ξ_1 and ξ_2 . These fields are assembled into an assumed solution for the position field

$$\mathbf{x}(\xi_1, \xi_2, \xi_3, t) = \mathbf{r}(\xi_3, t) + \xi_1 \mathbf{g}_1(\xi_3, t) + \xi_2 \mathbf{g}_2(\xi_3, t). \tag{9}$$

The director fields are illustrated in Figure 3. The deformation gradient for this field can be calculated by $\mathbf{F} = \frac{\partial \mathbf{x}}{\partial \mathbf{X}} = \frac{\partial \mathbf{x}}{\partial \xi} \frac{\partial \xi}{\partial \mathbf{X}_0} = \frac{\partial \mathbf{x}}{\partial \xi} \left(\frac{\partial \mathbf{X}_0}{\partial \xi} \right)^{-1}$, where \mathbf{X}_0 is the mapping from the ideal configuration ξ to the reference configuration \mathbf{X} . The gradient with respect to the ideal configuration is calculated from the ansatz by

$$\frac{\partial \mathbf{x}}{\partial \xi} = \left(\frac{\partial \mathbf{r}}{\partial \xi_3} + X_1 \frac{\partial \mathbf{g}_1}{\partial \xi_3} + X_2 \frac{\partial \mathbf{g}_2}{\partial \xi_3} \right) \otimes \hat{\mathbf{E}}_3 + \mathbf{g}_1 \otimes \hat{\mathbf{E}}_1 + \mathbf{g}_2 \otimes \hat{\mathbf{E}}_2. \tag{10}$$

If the unstrained configuration is assumed to be identical to the reference configuration, as is the case for the problem discussed later, the beam is initially straight with $\mathbf{X} = \xi$, $\frac{\partial \mathbf{X}}{\partial \xi} = \mathbf{I}$, and the deformation gradient is $\mathbf{F} = \frac{\partial \mathbf{x}}{\partial \xi}$. The deformation gradient and Jacobian with respect to this configuration are denoted by $\mathbf{F}_\xi = \frac{\partial \mathbf{x}}{\partial \xi}$ and $J_\xi = \det \mathbf{F}_\xi$, respectively. The unit vector along the centroid will be used and is defined in terms of the centroid position by

$$\mathbf{e}_{axis}(\xi_3) = \frac{d\mathbf{r}/d\xi_3}{\|d\mathbf{r}/d\xi_3\|_2}, \tag{11}$$

where $\|\cdot\|_2$ refers to the Euclidean norm, or two norm. In rotation-based beam models, this unit vector is obtained by applying the rotation matrix, \mathbf{R} , to the reference axis vector, $\mathbf{e}_{axis} = \mathbf{R}\hat{\mathbf{E}}_3$.

3.2. Balance of energy

The beams are assumed to have a constant temperature across their cross section, so that the temperature is only a function of the axis coordinate,

$$T = T(\xi_3). \tag{12}$$

This representation can be plugged into the balance of energy laws directly. The gradient in the reference configuration is then only constructed from the derivative along the centroid direction,

$$\nabla_{\xi} T = \frac{dT}{d\xi_3} \hat{\mathbf{E}}_3. \tag{13}$$

3.3. The restriction of electromagnetic problem to the beam

Without further assumptions, it would be necessary to mesh the space around the textile and calculate the electromagnetic fields there as well. The following assumptions allows for the consideration of only the electric field and current inside of the textile. The base assumption to the electromagnetic discretization is that the conduction current density is uniform across the cross section and oriented along the axis of the beam, such that

$$\mathcal{J} = \mathcal{J}(\xi_3) \mathbf{e}_{axis}(\xi_3). \tag{14}$$

Assuming isotropy, the constitutive law $\mathcal{J} = \sigma \mathcal{E}$ requires that the electromotive intensity must also be oriented along the axis of the fibril, yielding the relations $\mathcal{E} \cdot \mathbf{F}_{\xi} \hat{\mathbf{E}}_1 = \mathcal{E} \cdot \mathbf{F}_{\xi} \hat{\mathbf{E}}_2 = 0$. When considering the PDE in the ideal coordinate frame, only the ξ_3 direction is not trivially satisfied, so the one-dimensional PDE that needs to be solved is

$$\frac{\partial}{\partial \xi_3} \sigma_{\xi} \frac{\partial V}{\partial \xi_3} = 0. \tag{15}$$

Thus, for computation purposes, only the voltage at the centroid of the beam needs to be solved, yielding an unknown field that is only a function of the axis coordinate,

$$V = V(\xi_3). \tag{16}$$

Because the only nonzero component of \mathcal{E} is along the axis coordinate, the conduction current density in the laboratory frame can be determined to depend on the laboratory frame voltage by

$$\mathcal{J} = \frac{1}{J_{\xi}} \mathbf{F}_{\xi} \sigma_{\xi} \left(-\frac{\partial V}{\partial \xi_3} \right) \hat{\mathbf{E}}_3. \tag{17}$$

4. CONTACT TREATMENT

4.1. Surface mapping

To integrate the contact problem into a general finite element framework, contacts can be viewed on a surface of discontinuity. The treatment of the constitutive responses of the surfaces can be described using jump conditions on the change in fields across the two material bodies. One body can be referred to as the + surface and the other as the - surface, where the normal vector \mathbf{n} will be defined to point towards the + surface, as illustrated in Figure 4. Each body has two separate

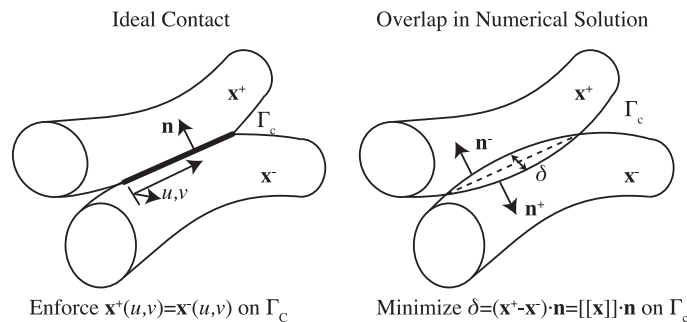


Figure 4. Contact constraint.

deformation fields and two separate reference configurations, $\mathbf{x}^+ = \boldsymbol{\chi}^+(\mathbf{X}^+)$ and $\mathbf{x}^- = \boldsymbol{\chi}^-(\mathbf{X}^-)$. The surface can be parametrized by two coordinates, u, v , with its own position function $\mathbf{x}_c = \mathbf{x}_c(u, v)$. Ideally, on a contact, the two surfaces will be coincident and have the same spatial coordinates, that is,

$$\mathbf{x}_c(u, v) = \mathbf{x}^+(u, v) = \mathbf{x}^-(u, v) \text{ on } \Gamma_c. \tag{18}$$

The condition that the surfaces are coincident is weakened to enable finding finite element solutions to satisfy it. As illustrated in Figure 4, the approximate solutions to each body will be allowed to overlap slightly. The contact region Γ_c is the portion on each surface where the two bodies overlap. The mapping between the two surfaces is needed, as they are no longer coincident, and the contact region is now considered to be two connected surfaces. The region is defined as pairs of points on each surface that are inside of the other body that are the closest to one another. That is, for each point on the boundary of one body and inside the other body, its connected point is the closest point on the other body's surface. The geometry can be defined by and constructed by

$$\Gamma_c = \left\{ (\mathbf{x}^+, \mathbf{x}^-) \mid \forall \mathbf{x}^+ \in (\partial\Omega^+ \cap \Omega^-), \mathbf{x}^- = \arg \min_{\mathbf{x}^- \in (\Omega^+ \cap \partial\Omega^-)} |\mathbf{x}^+ - \mathbf{x}^-| \right\} \tag{19}$$

and is illustrated in Figure 6. This object directly translates into a table of quadrature point pairs in the finite element implementation; the procedure for its construction is described in Section 4.4. The jump in the spatial coordinate on the contact region is equal to $\llbracket \mathbf{x} \rrbracket = \mathbf{x}^+ - \mathbf{x}^-$.

4.2. Constitutive laws

The contact region represents a surface of discontinuity for all of the fields that exist on the two bodies. Thus, constitutive responses for the tractions, heat fluxes, and surface currents need to be specified, which are functions of the jumps in the fields,

$$\{\mathbf{t}, q_n, \mathcal{J}_n\} = f(\llbracket \mathbf{x} \rrbracket, \llbracket T \rrbracket, \llbracket V \rrbracket). \tag{20}$$

They may all be dependent on one another; particularly, the contact pressure has significant effects on both thermal and electric contact resistances [39]. For simplicity, only linear and independent contact laws are considered. For the tractions, a simple penalty term with a sufficiently large parameter P^* is used to penalized the overlap,

$$\mathbf{t} = P^* (\llbracket \mathbf{x} \rrbracket \cdot \mathbf{n}) \mathbf{n}. \tag{21}$$

The two bodies are also placed in thermal contact, so a jump condition is needed to relate the heat flux across the bodies that is dependent on the jump in temperature. Linear thermal contact resistances have the form

$$\mathbf{q} = h_c \llbracket T \rrbracket \mathbf{n}, \tag{22}$$

where h_c is the contact heat transfer coefficient. Similarly, for the electromagnetic problem, a contact resistance appears with a surface conductivity σ_c that relates the current across the surface to the potential drop across the surface,

$$\mathcal{J} = \sigma_c \llbracket V \rrbracket \mathbf{n}. \tag{23}$$

4.3. Beam geometry

The beam-based theory has a particular geometry representation that needs to be taken into account to handle the contacts. The geometry is illustrated in Figure 5. Because the finite element meshes are one-dimensional along the axis, instead of preventing an overlap of two solid finite element

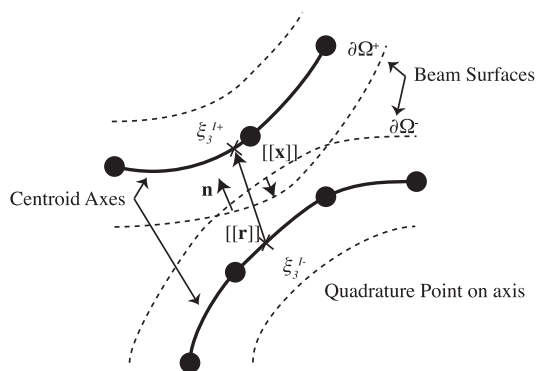


Figure 5. Contact geometry for beams.

meshes, the penalty must be designed to keep two one-dimensional meshes a minimum distance apart from one another. The distance between centroid axes, which are represented by the finite element meshes, always remains positive, and an overlap between beams corresponds to the distance dropping below a threshold value, for example, $R^+ + R^-$.

Three simplifications are currently used when performing the geometric calculations:

- (1) The centroid interpolation is linear even if higher-order elements are being used (the elements of the mesh are always line segments).
- (2) The cross sections do not deform and remain circular.
- (3) The contact area can be approximated with a cylinder–cylinder Hertzian response.

These simplifications were only made to reduce the computational cost and reduce the implementation complexity and are not a limitation of the beam formulation; it is possible to construct more detailed calculations for deformed higher-order beam surfaces. The first two simplifications enable an analytical solution to be found for one unknown, instead of a Newton iteration being required to simultaneously solve for five unknowns (the three coordinates on the ‘-’ beam and the cross-section coordinates on the surface of the ‘+’ beam.)

The closest point mapping reduces to the equation

$$\xi_3^- = \arg \min_s |\mathbf{r}^+(\xi_3^+) - \mathbf{r}^-(s)| \tag{24}$$

with variable of optimization s . When constructing the contact mapping, equally spaced points are placed along one element on ‘+’ beam, and the closest point on the ‘-’ beam is found. The normal component at the surface of the two beams is calculated using only the centroid positions,

$$\mathbf{n} = \frac{[[\mathbf{r}]]}{\|[[\mathbf{r}]]\|_2}, \tag{25}$$

which points out from the ‘-’ beam into the ‘+’ beam. Using that assumption, the overlap in the kinematic displacement fields is defined just by the centroid positions:

$$[[\mathbf{x}]] = (R^+ + R^- - (\mathbf{r}^+(\xi_3^+) - \mathbf{r}^-(\xi_3^-)) \cdot \mathbf{n}) \mathbf{n} = (2 \langle R \rangle - \|[[\mathbf{r}]]\|_2) \mathbf{n}. \tag{26}$$

The beam meshes are only one-dimensional, so the integrals that will be evaluated will be one-dimensional along the centroid of the beam. The integral of the jump condition over the entire contact area is required, so a differential line thickness a at a contact pair ξ_3^+, ξ_3^- is required to transform the area integral into a one-dimensional integral:

$$\int_{\Gamma_c} dA = \int_{\xi_3 \in \Gamma_c} a d\xi_3. \tag{27}$$

The mechanical analysis will be acceptable without considering the contact area because the penalty parameter is chosen to be arbitrary. Thus, the penalty condition can be stated as

$$\int_{\Gamma_c} \mathbf{f} \cdot \mathbf{n} dA = \int_{\xi_3 \in \Gamma_c} P^* [\mathbf{x}] \cdot \mathbf{n} d\xi_3. \tag{28}$$

However, the thermal and electrical contacts do use jump conditions with physical origins, so the contact area is required for consistency. The dependence on contact area gives an implicit coupling between the mechanical fields and the thermal and electric contacts: Increasing the contact pressure increases the contact area, which in turn decreases the contact resistances, even when not considering tribological effects (indeed, at the textile macroscale, this contact area dependence is a tribological effect). Because of the arbitrary nature of the penalty, the overlap distance is nonphysical. The contact pressure, which is a physical quantity, can be used to calculate an appropriate contact area. Hertzian contact theory can be used as an adequate approximation using the case of two parallel cylinders, $a = \sqrt{\frac{4PR^*}{\pi E^*}}$, where R^* and E^* are the effective radius and the Young's modulus, respectively, between the two cylinders [40]. These quantities are calculated by $E^* = \left(\frac{E^+}{1-\nu_+^2} + \frac{E^-}{1-\nu_-^2} \right)^{-1}$ and $R^* = (R_+^{-1} + R_-^{-1})^{-1}$. The total differential load is denoted by P , that is, the integral of the traction along a differential line element of the contact surface, $P(\xi_3) = \int_{d\Gamma_c(\xi_3)} \mathbf{t}(\xi_3) \cdot \mathbf{n} ds$. This is recognized as the penalty jump condition, $P(\xi_3) = P^* [\mathbf{x}] \cdot \mathbf{n}$. This enables the differential thickness to be written as

$$a = \sqrt{\frac{4R^*}{\pi E^*} (P^* [\mathbf{x}] \cdot \mathbf{n})}. \tag{29}$$

Then, the differential contributions of the thermal and electrical jump conditions can be expressed along the differential line element $d\xi_3$,

$$h_c [T] dA = h_c [T] \sqrt{\frac{4R^*}{\pi E^*} (P^* [\mathbf{x}] \cdot \mathbf{n})} d\xi_3, \tag{30}$$

$$\sigma_c [V] dA = \sigma_c [V] \sqrt{\frac{4R^*}{\pi E^*} (P^* [\mathbf{x}] \cdot \mathbf{n})} d\xi_3, \tag{31}$$

coupling them nonlinearly to the mechanical field.

4.4. Contact mapping generation

For each pair of contacting meshes, a discrete contact mapping needs to be constructed. The continuous contact zones are discretized as tables of quadrature points for nearby elements, illustrated in Figure 6. The discrete mapping is represented as a list of active interacting element pairs and

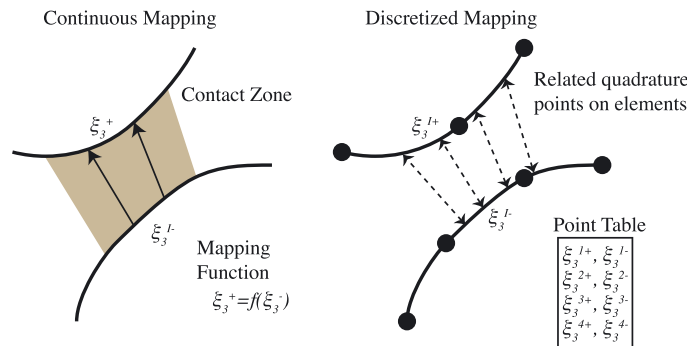


Figure 6. Discretized contact mapping.

a corresponding quadrature point table. The quadrature point table for each active pair has $2N_{GP}$ entries: one list of points on the ‘+’ element and a corresponding list of points on the ‘-’ element. The quadrature points are indexed by I , so that each contact maintains a list of pairs (ξ_3^{I+}, ξ_3^{I-}) for $I = 1 \dots N_{GP}$. A fibril assembly consists of many independent meshes that can all be contacting independently. One such list of element pairs exists for every interacting pair of meshes as well. The quadrature point table is determined by picking equally spaced points along the ‘+’ element and finding the closest point on the ‘-’ element. Using linear shape functions, the displacement field along the element on the - beam can be described as $\mathbf{r}^-(s) = s\mathbf{r}_1^- + (1-s)\mathbf{r}_2^-$ with $s \in [0, 1]$, where \mathbf{r}_1^- and \mathbf{r}_2^- are the values at the two nodes (1 and 2) of the element. From Equation 24, the arg min problem, with variable s , with this discretization is

$$\xi_3^{I-} = \arg \min_s \left| \mathbf{r}^+ (\xi_3^{I+}) - s\mathbf{r}_1^- - (1-s)\mathbf{r}_2^- \right|. \tag{32}$$

This equation can be solved analytically for the corresponding point

$$s_I^- = \frac{(\mathbf{r}_2^- - \mathbf{r}_1^-) \cdot (\mathbf{r}_I^+ - \mathbf{r}_2^-)}{(\mathbf{r}_2^- - \mathbf{r}_1^-) \cdot (\mathbf{r}_2^- - \mathbf{r}_1^-)}, \tag{33}$$

given one of the equally spaced points $\mathbf{r}_I^+ = \mathbf{r}^+ (\xi_3^{I+})$, thus producing one of the required quadrature point pairs.

5. VARIATIONAL FORM

For the beam formulation, the sought function of the director fields is taken as the set of the three unknown fields, denoted by $x = \{\mathbf{r}, \mathbf{g}_1, \mathbf{g}_2\}$. The velocity of the director fields is denoted by prefixing with a \mathbf{v} , so that the unknown velocity functions are $v = \{\mathbf{v}\mathbf{r}, \mathbf{v}\mathbf{g}_1, \mathbf{v}\mathbf{g}_2\}$. Because the function spaces for the position and velocity are the same, so are the test functions $\delta x = \delta v = \{\delta\mathbf{r}, \delta\mathbf{g}_1, \delta\mathbf{g}_2\}$. Similarly to the displacement, the velocity field is constructed as $\mathbf{v}(t, \xi_1, \xi_2, \xi_3) = \mathbf{v}\mathbf{r}(t, \xi_3) + \xi_1\mathbf{v}\mathbf{g}_1(t, \xi_3) + \xi_2\mathbf{v}\mathbf{g}_2(t, \xi_3)$, and the test on displacements is constructed by $\delta\mathbf{x}(\xi_1, \xi_2, \xi_3) = \delta\mathbf{r}(\xi_3) + \xi_1\delta\mathbf{g}_1(\xi_3) + \xi_2\delta\mathbf{g}_2(\xi_3)$.

The integration over the domain is split between the cross section and the axis. The finite element approximation discretizes the solution along ξ_3 , and the integral along the length of the beam $\int_0^L d\xi_3$ is handled by the finite element program, where the domain is written as $\xi_3 \in [0, L]$. Integration over the cross section is evaluated by Gaussian quadrature, so that each Gauss point on the finite element discretization maps to multiple Gauss points on the cross section and its boundary. Let $w^A, \hat{\xi}^A \in P(\Omega)$ denote the set of Gauss points and weights over the geometric quantity Ω , which will be the cross section at a particular point along the beam, $C(\xi_3)$, and its boundary, $\partial C(\xi_3)$.

The integrations take place by summing the contributions between each mesh and each set of active contact regions. Let M denote an individual mesh, $\{M\}$ denote the set of all meshes in the problem, and $\{\Gamma_c\}$ denote the set of all contact regions. The variational form used to assemble the mass matrix for all the fibrils is

$$\mathbb{M}_m(\delta x, \dot{v}) = \sum_{M \in \{M\}} \int_0^L \sum_{A \in P(C)} w^A (\delta\mathbf{r} + \xi_1^A \delta\mathbf{g}_1 + \xi_2^A \delta\mathbf{g}_2) \cdot \rho \left(\dot{\mathbf{v}}\mathbf{r} + \xi_1^I \dot{\mathbf{v}}\mathbf{g}_1 + \xi_2^I \dot{\mathbf{v}}\mathbf{g}_2 \right) d\xi_3, \tag{34}$$

and the loading vector as a sum of all the fibril domains and contact surfaces is

$$\begin{aligned} \mathbb{F}_m(\delta x, x, v; T, V) = & \sum_{M \in \{M\}} \left(\int_0^L \sum_{A \in P(C)} w^A \delta\mathbf{x} \cdot \frac{\delta\psi}{\delta\mathbf{x}} d\xi_3 + \left[\sum_{A \in P(C)} w^A \delta\mathbf{x} \cdot \bar{\mathbf{p}} \right]_0^L \right) \\ & + \sum_{\Gamma_c \in \{\Gamma_c\}} \left(\int_{\xi_3 \in \Gamma_c} \llbracket \delta\mathbf{r} \rrbracket \cdot P^* (2(R) - \llbracket \mathbf{r} \rrbracket \llbracket \mathbf{r} \rrbracket_2) \mathbf{n} d\xi_3 \right). \end{aligned} \tag{35}$$

The time-dependent variational problem for the mechanical system is then

$$\mathbb{M}_m(\delta x, \dot{v}) = \mathbb{F}_m(\delta x, x, v; T, V) \forall \delta x. \tag{36}$$

The variational form for thermal problem is

$$\begin{aligned} \mathbb{F}_T(\delta T, T; v, x, V) = & \sum_{M \in \{M\}} \int_0^L \sum_{A \in P(C)} w^A \left(\frac{d\delta T}{d\xi_3} k_0 \frac{dT}{d\xi_3} + \delta T \frac{\mathcal{J}^2}{\sigma_0} \right) d\xi_3 \\ & + \sum_{M \in \{M\}} \left[\sum_{A \in P(C)} w^A \delta T \cdot \bar{q}_{0n} \right]_0^L + \sum_{\Gamma_c \in \{\Gamma_c\}} \left(\int_{\xi_3 \in \Gamma_c} \llbracket \delta T \rrbracket h \llbracket T \rrbracket a d\xi_3 \right), \end{aligned} \tag{37}$$

which satisfies $0 = \mathbb{F}_T(\delta T, T; x, v, V) \forall \delta T$ in the static case, and the variational form for the voltage problem is

$$\begin{aligned} \mathbb{F}_V(\delta V, V; v, x, T) = & \sum_{M \in \{M\}} \left(\int_0^L \sum_{A \in P(C)} w^A \frac{d\delta V}{d\xi_3} \sigma_0 \frac{dV}{d\xi_3} d\xi_3 + \left[\sum_{A \in P(C)} w^A \delta V \cdot \bar{J} \right]_0^L \right) \\ & + \sum_{\Gamma_c \in \{\Gamma_c\}} \left(\int_{\xi_3 \in \Gamma_c} \llbracket \delta V \rrbracket \sigma_c \llbracket V \rrbracket a d\xi_3 \right), \end{aligned} \tag{38}$$

which satisfies $0 = \mathbb{F}_V(\delta V, V; x, v, T) \forall \delta V$ in both the static and time-dependent cases.

6. REPRESENTATIVE VOLUME ELEMENT SETUP AND ANALYSIS

6.1. Homogenization

In a plain-woven fabric, yarns are laid out in two directions, called the warp and weft direction. A 4 yarn by 4 yarn unit cell is used to negate the effects of boundary conditions. The microstructure creates an inherently anisotropic unit cell for a continuum model. The deformation of the fibrils at the microscale creates cross couplings between the mechanical fields and the thermal and electrical fields, so that the bulk conductivities and permittivities will be strain dependent. A continuum model could also be developed for the electric responses, for example, using the homogenization procedure described by Kuznetsov [10]. However, this would be too broad to model patterns of insulating fibrils and conducting fibrils required for some applications, such as complex electronic circuits. Another strategy is to model each unit cell as an electrical network with property-dependent resistors, with a one-to-one mapping between unit cells and network cells. A network model can be more readily incorporated into standard electric circuit analysis methods. For example, see Tao [41] for the development of resistor network model from experimental data. The homogenization process is illustrated in Figure 7.

At the microscale level, the stress, displacement, heat flux, and thermal fields are locally variable. Because the textile unit cell is made up of discrete bodies, the average traction on a boundary is calculated by a summation,

$$\langle \mathbf{t} \rangle = \frac{1}{|\Gamma_0|} \sum_{fibrils} \int_{\Gamma_0} \mathbf{P} \mathbf{N} d\Gamma, \tag{39}$$

which is related to the total force on the boundary by $\mathbf{f} = |\Gamma_0| \langle \mathbf{t} \rangle$, where $|\Gamma_0|$ is the area of the domain and \mathbf{N} is the surface normal in the reference configuration. This will be used to produce an effective constitutive response for the unit cell by producing two sets of data

$$\mathbf{f}_{warp} = \hat{f}_{warp}(\langle \mathbf{C} \rangle) = \sum_{M \cap \Gamma_{warp}} \int_{\Gamma_{warp}} \mathbf{P} \hat{\mathbf{E}}_1 d\Gamma, \tag{40}$$

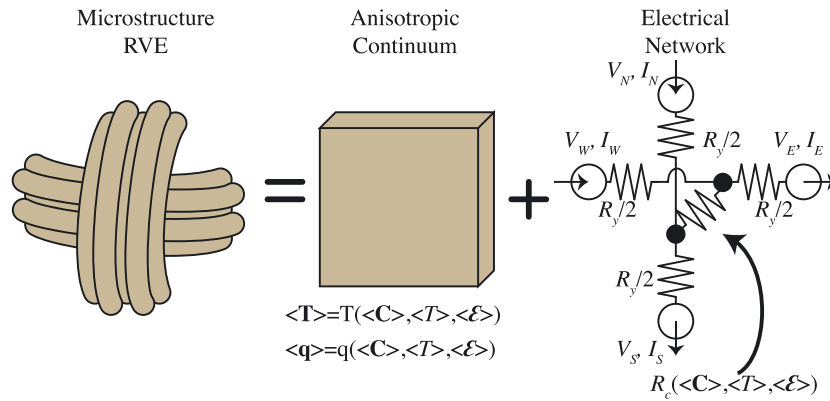


Figure 7. Homogenization of a microstructure into an anisotropic solid and an electrical network. RVE,.

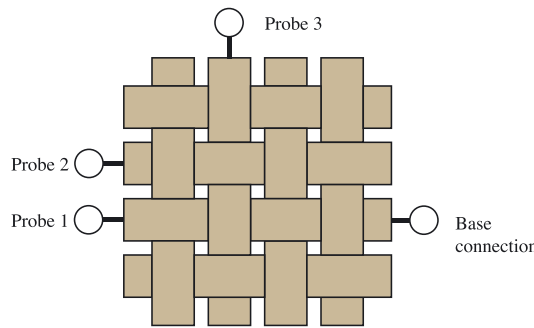


Figure 8. Probe locations.

$$\mathbf{f}_{wef t} = \hat{f}_{wef t}(\langle \mathbf{C} \rangle) = \sum_{M \cap \Gamma_{wef t}} \int_{\Gamma_{wef t}} \mathbf{P} \hat{\mathbf{E}}_2 \, d\Gamma \tag{41}$$

for each side of the unit cell, which are functions of the average stretch state of the cell, $\langle \mathbf{C} \rangle$. The same process can be performed on the heat flux to produce a constitutive response for the heat flux as a function of applied temperature gradients at the current stress state, $\langle \mathbf{q} \rangle = \hat{q}(\langle \nabla_x T \rangle; \langle \mathbf{C} \rangle)$, but the response not of interest for this example.

6.2. Electrical network fitting

Creating an electrical network model does not require any averaging operations. It is required to obtain the total current that passes through the unit cell in response to an applied voltage difference. The applied voltage is the same on the macroscale and microscale. The total current is obtained by integrating the current density along the boundaries of the domain corresponding to the probe locations,

$$I = \int_{\Gamma_1} \mathcal{J} \cdot \mathbf{n} \, d\Gamma = - \int_{\Gamma_{ground}} \mathcal{J} \cdot \mathbf{n} \, d\Gamma = - \sum_{M \cap \Gamma_B} \int_{\Gamma_B} \mathcal{J} \cdot \mathbf{n} \, d\Gamma, \tag{42}$$

which should be equal and opposite if a simple current path is considered. The resulting currents through three electrical paths are determined: (1) straight through the same yarn; (2) between two parallel yarns; and (3) two perpendicular yarns. The probe locations are illustrated in Figure 8.

With the network model illustrated in Figure 7, the RVE contains 16 unit cells, so that the network is 16×2 yarn resistors and 16×4 contact resistors. Assuming that there are only two types of resistors that see the same input stress state across all of the unit cells—the resistance through a yarn segment, $R_y(\langle \mathbf{C} \rangle)$, and the effective contact resistance between yarns, $R_c(\langle \mathbf{C} \rangle)$ —the three probes can be used to calculate the resistances for the unit cell.

Applying Kirchhoff's laws to a single unit cell yields four equations

$$0 = \frac{R_y}{2} I_W + \frac{R_y}{2} I_E + V_E - V_W, \tag{43}$$

$$0 = \frac{R_y}{2} I_N + \frac{R_y}{2} I_S + V_S - V_N, \tag{44}$$

$$0 = R_c (I_W - I_E) + \frac{R_y}{2} I_W - \frac{R_y}{2} I_N + V_N - V_W, \tag{45}$$

$$0 = R_c (I_S - I_N) + \frac{R_y}{2} I_W - \frac{R_y}{2} I_N + V_N - V_W \tag{46}$$

that depend on the voltages and currents at the north, west, south, and east connections of the cell. These unit cells are connected in a grid to complete the network model that given boundary conditions and values for R_c and R_y can be used to solve for V_{ij} and I_{ij} , values indexed by the network grid location ij . The 'nodes' in this model have an associated cross section, so that the current at a node is the total current passing across the yarn cross section out of 1 unit cell into the neighboring unit cell. The boundary conditions for the network problem are $V = 0V$ at the node for the ground pad, $V = 1V$ at the node for probe location, and $I = 0$ at all other boundary nodes. The currents at the voltage boundary conditions are unknown and are the sought quantity. One configuration of the network has 64 unknowns of voltages and currents at nodes.

Given the boundary condition configurations associated with probe location p and trial values for R_y and R_c , the output current I_{net}^p can be calculated by solving the entire network for V_{ij}^p and I_{ij}^p . A minimization problem can then be solved over the three probe locations using the calculated currents from the simulation, I_{sim}^p , to determine the resistances that best match the simulation, which would ideally satisfy $I_{net}^p(R_y, R_c) = I_{sim}^p$, $p = 1, 2, 3$. The errors in current for all three probe setups are minimized simultaneously to solve for a single pair of resistor values that best approximates the behavior of the simulation,

$$R_y, R_c = \arg \min_{s,r} \sqrt{(I_{net}^1(s, r) - I_{sim}^1)^2 + (I_{net}^2(s, r) - I_{sim}^2)^2 + (I_{net}^3(s, r) - I_{sim}^3)^2}. \tag{47}$$

This process is repeated for each solved stretch state to produce a function for the resistances given one of the simulated states, $R_y ((C))$ and $R_c ((C))$.

6.3. Analysis methodology

Dynamic relaxation is used to guide the solution towards a static solution. The velocity dependence prevents—or at least mediates—convergence issues caused by the onset of contacts and the lack of stiffness normal to the plane of the fabric and axis of the beams. Dynamic relaxation has been used in the study membranes, for example, Haseganu [42]. Further, because of the very large deformations and steep contact penalties, the problem is not smooth enough to solve with standard nonlinear static analysis. An external dissipation force density is applied to the beam to bring it towards a steady state, equal to

$$\mathbf{f} = -\gamma \mathbf{v}, \tag{48}$$

where γ is positive and large enough to make the motion critically damped. This value is determined by trial and error to produce a stable simulation while still relaxing as quickly as possible to the steady state. The dynamic equations are marched in time using backward Euler, which provides additional stability and dampening that are beneficial to dynamic relaxation.

States of the material after heavily dampened relaxation times are taken to be the equilibrium states of the material. Only the mechanical fields are solved dynamically. At each equilibrium state after relaxing the mechanical fields, the electrical and thermal problems are solved statically for

Algorithm 1 Sampling procedure using dynamic relaxation

1. Find the next equilibrium position for sampling:
 - (a) Set the velocity field to a given strain rate.
 - (b) Solve the dynamic problem—only solving for the mechanical fields—for t_{step} time.
 - (c) Set the velocity field to zero.
 - (d) Solve the dynamic problem with a large dampening parameter for t_{relax} time.
2. Record reaction forces and electric currents:
 - (a) Set the velocity field to zero.
 - (b) Integrate $\mathbf{f} = \sum_I \int_{\Gamma_I} \mathbf{P} \cdot \mathbf{E}_3 d\Gamma$ to determine the total reaction force on desired boundaries.
 - (c) For each set of probe locations:
 - (i) Set the voltage field to match the desired probe values
 - (ii) Solve the electric potential problem with the relaxed mechanical fields with applied potential boundary conditions
 - (iii) Integrate $I = \sum_I \int_{\Gamma_I} \mathcal{J} \cdot \mathbf{e}_y d\Gamma$ to determine the total current on desired boundaries.
 - (iv) Solve the thermal problem
 - (v) Save fields to a file
3. Repeat until all desired samples have been taken.

each configuration of electrical probes, given the current deformation and contact state. The sampling procedure is detailed in Algorithm 1. This system only works assuming a one-way coupling between the mechanical state of the material and the thermal and electric fields. If more complicated constitutive laws are considered, the thermal and electric problems need to be varied independently, so that many more samples of the material state would be needed.

In the mechanical analysis, the centroids are pinned at their initial condition. The cross sections are free to pivot to allow the yarns to reorient so that there is a no-applied-torque boundary condition on the directors. The boundary conditions can be written for the strong-form problem as

$$\Delta \mathbf{v}\mathbf{r} = \mathbf{0} \text{ on } \partial\Omega, \quad (49)$$

$$\int_A \xi_1 \bar{\mathbf{t}} d\Gamma = \mathbf{0} \text{ on } \partial\Omega, \quad (50)$$

$$\int_A \xi_2 \bar{\mathbf{t}} d\Gamma = \mathbf{0} \text{ on } \partial\Omega, \quad (51)$$

where $\Delta \mathbf{v}\mathbf{r}$ is the Newton update on the velocity.

The voltage field has Dirichlet boundary conditions only on the probe locations: the base connection Γ_B and the probe location Γ_P . The probe domain Γ_P matches one of the three locations illustrated in Figure 8. Even though the problem for the potential happens to be linear in this case, the same Newton's method solver as the mechanical system is used for both ease of implementation and to allow for nonlinear effects in the future. The desired values for the Dirichlet boundary conditions are set via an initial condition, and the boundary conditions applied to the matrix system are on the Newton update, which must be set to zero. The remaining boundaries are insulating so that $\bar{\mathbf{J}} \cdot \mathbf{n} = 0$. The boundary conditions on the PDE are

$$\Delta V = 0 \text{ on } \Gamma_B \text{ and } \Gamma_P, \quad (52)$$

$$-\bar{\mathbf{J}} \cdot \mathbf{n} = \sigma \nabla_x V \cdot \mathbf{n} = 0 \text{ on } \partial\Omega \setminus (\Gamma_B \cup \Gamma_P), \quad (53)$$

where ΔV is the Newton update on the voltage. The effect of Joule heating in the fabric is based on the calculated currents is also observed. The temperature is pinned to zero (difference from the

reference temperature) on the boundaries. Similarly to the electric potential, the boundary conditions are set with initial conditions, and the boundary condition for the matrix system is a zero update,

$$\Delta T = 0 \text{ on } \partial\Omega. \quad (54)$$

7. IMPLEMENTATION

The code is dependent upon the finite element package FEniCS [35]. Its code generation features—especially automatic differentiation—make it an appealing choice. These features greatly facilitated the development of multiphysics beam formulations with implicit time stepping. A number of patches were made to the FEniCS code base to support contact mechanics, specifically Dolfin [43] and FEniCS Form Compiler (FFC) [44]. These patches are described in detail in Queiruga [45] and briefly described here. The custom integral syntax in FEniCS was extended with an identifying tag that tells the patches to FFC to generate integration routines for a contact. Custom assembly code was implemented as a C++ extension to generate quadrature points and assemble over element pairs. The existing analysis and differentiation algorithms in FFC perform all of the expression manipulations required, and most of the new capabilities and modifications were centered in the code generation components.

The code also makes use of Numpy [46] and Scipy [47] for the *de facto* standard Python numerical array data type and numerical algorithms, Mathematica [48] for code generation and symbolic integration and differentiation, Matplotlib [49] for plotting, and Paraview [50] for visualization. The network model and error minimization described in Section 6.2 are implemented in Mathematica as well.

8. RESULTS

8.1. Properties

In this example, all of the fibrils are the same. The properties are listed in Table I. The initial configuration, used to generate the woven structure, and the relaxed state, after the first pass of dynamic relaxation, are shown in Figure 9. The reference configurations of each of the fibrils are straight, and

Table I. Simulation parameters for plain woven fabric.

Unit cell width	W	8 mm	Electrical conductivity	σ	$10 \frac{\text{S}}{\text{mm}}$
Density	ρ	$1.0 \frac{\text{g}}{\text{mm}^3}$	Thermal conductivity	k	$1.0 \frac{\text{W}}{\text{mmK}}$
Young's modulus	E	1.26 MPa	Thermal contact conductivity	h_c	$0.1 \frac{\text{W}}{\text{mm}^2\text{K}}$
Poisson's ration	ν	0	Electrical contact conductivity	σ_c	$0.01 \frac{\text{A}}{\text{mm}^2\text{V}}$
Fibril radius	R	0.15 mm	Contact penalty coefficient	P^*	$5 \frac{\text{N}}{\text{mm}}$
Dissipation	γ	$0.1 \frac{\text{Ns}}{\text{m}}$			

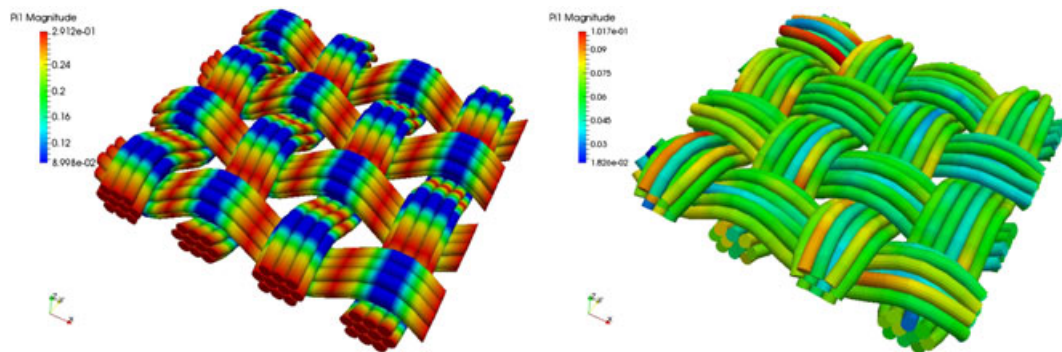


Figure 9. Initial condition geometry (left) and dynamically relaxed geometry (right). The mesh is colored by the total reaction force across the cross section, $\int_C(\xi_3) \mathbf{P}\mathbf{E}_3 dA$, measured in newtons.

the fibrils would intersect with crossing fibrils if started from the reference configuration. Each yarn is initially in a three-level stack of with a 3-4-3 fibril count pattern (see the bottom left of Figure 9.) After the relaxation process, it is observed in the cross section through one of the center yarns that the yarns flatten out into a two-level stacking, shown in Figure 10.

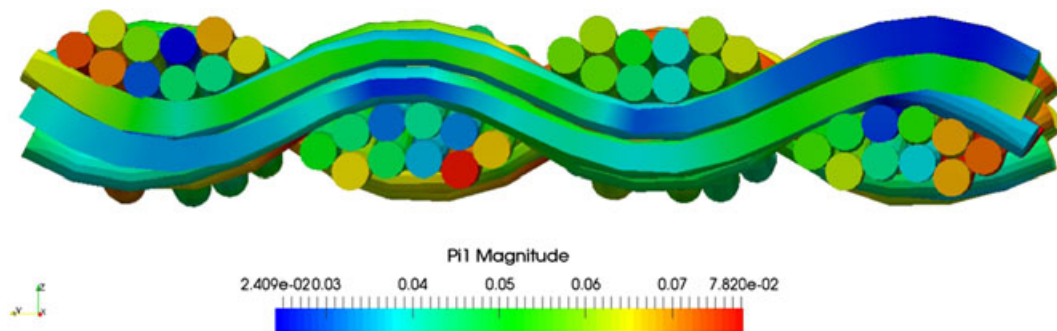


Figure 10. Cross section of relaxed plain weave. The internal reaction force is measured in newtons.

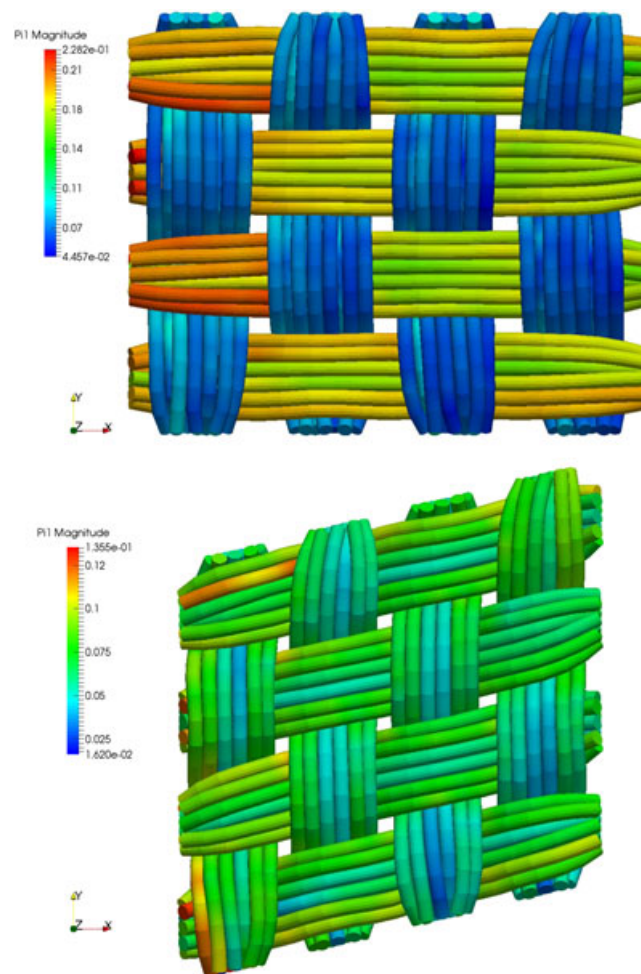


Figure 11. Final stress distributions at 25% strain for stretching (top) and shearing (bottom). The reaction force is measured in newtons.

8.2. Mechanical behavior

Two deformations are considered: uniaxial extension and simple shearing. The velocity field used to drive uniaxial extension/compression (step 1a in Algorithm 1) is

$$\mathbf{v} = \frac{\Delta_{step}}{t_{step}} \frac{X_1}{L_0} \mathbf{e}_1, \tag{55}$$

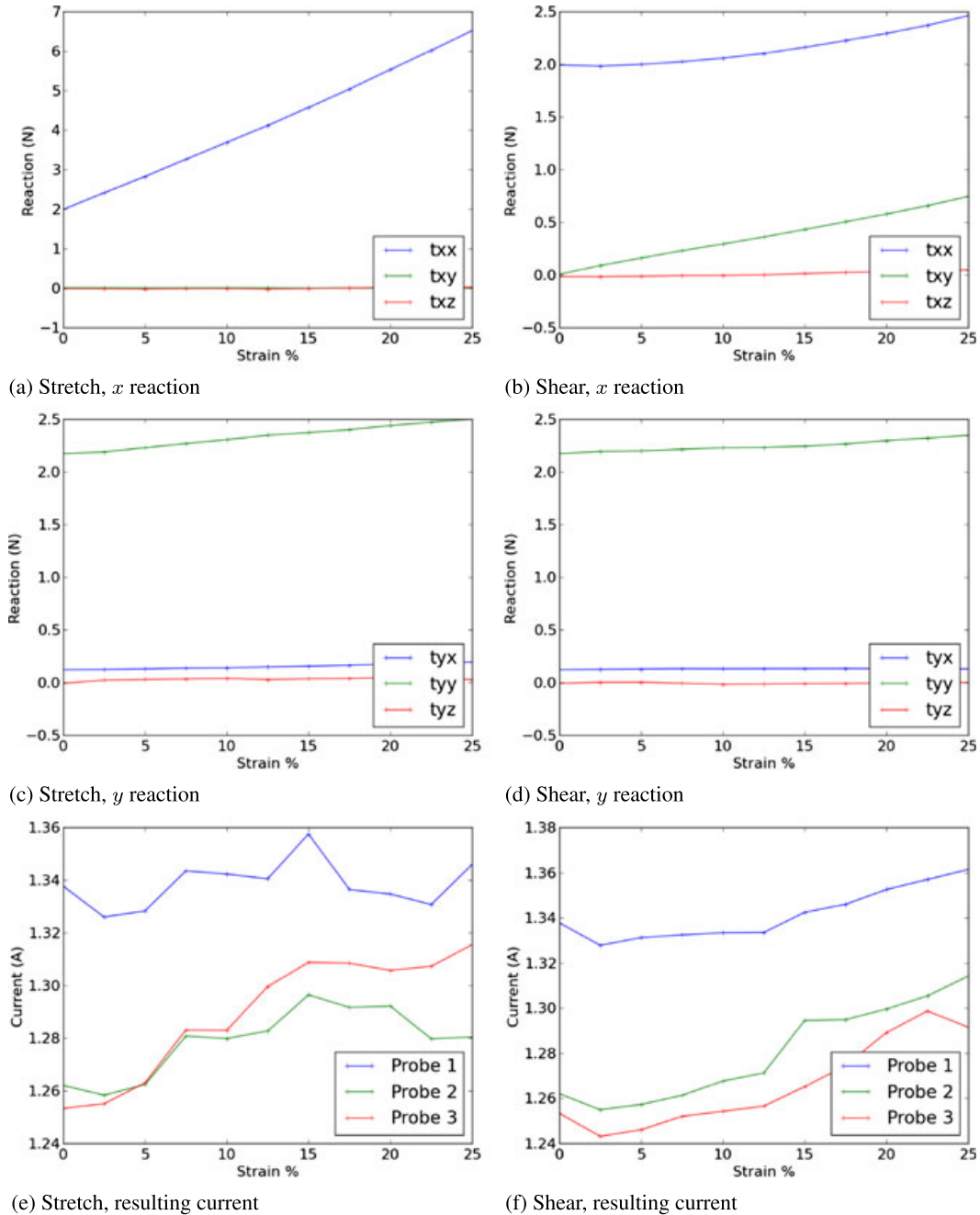


Figure 12. Reaction forces and currents for the uniaxial stretching case (left) and the shear case (right). A test voltage of 1 V is applied, so the effective electrical resistance is the reciprocal of the measured currents. (a) Stretch, x reaction, (b) shear, x reaction, (c) stretch, y reaction, (d) shear, y reaction, (e) stretch, resulting current, and (f) shear, resulting current.

and the velocity field used to drive the simple shearing is

$$\mathbf{v} = \frac{\Delta_{step}}{t_{step}} \frac{X_1}{L_0} \mathbf{e}_2. \quad (56)$$

In these equations, Δ_{step} is the desired strain to be applied during the step over the course of t_{step} time. The unit cell is brought to 25% strain over the course of 10 steps for both cases. The final strained states are rendered in Figure 11. The calculated force and current responses for both cases are plotted in Figure 12. The z direction corresponds to out-of-plane reactions. Because only in-plane motion is considered, the reaction forces stay near zero in this component.

The end points of each of the fibrils are held fixed at the reference length. Because of the interweaving, this places each fibril in tension, although the stress fields are not uniform as seen in Figures 9 and 10. Some fibrils in the corners have particularly high stresses, such as the one visible at the top of the figure, where they are unable to move because of the pinned boundary conditions. The unit cell is thus originally in tension, with approximately 2 N of force acting on the clamps in both directions. A relaxation process could be applied in which the yarns at the boundary were allowed to move inwards to bring the initial tractions to zero, but is not carried out in this example.

8.3. Electrical behavior

The current distributions through the fabric in these deformed states are shown in Figure 13. The temperature distributions in the unit cell due to the Joule heating effect are shown in Figure 14. As can be seen in Figure 13, an appreciable amount current passes through neighboring yarns in all cases. A larger current corresponds to a lower resistance.

The values for the two resistors, R_y ($\langle C \rangle$) and R_c ($\langle C \rangle$), obtained from this calculation are shown in Figure 15 along side the value for R_y expected from the insulated case. The trend in the contact resistance matches with the trend seen in the currents in Figure 12(e) and (f).

The resistance of a single yarn segment can be calculated analytically by N_{fib} cylindrical conductors in parallel,

$$R_y = \frac{W/N_{cell}}{\sigma \pi R_{fib}^2 N_{fib}} = \frac{8 \text{ mm}/4}{10 \frac{\text{s}}{\text{mm}} \pi (0.15 \text{ mm})^2 10} \approx 0.282 \Omega. \quad (57)$$

As a sanity check, the electrical voltage calculation was performed with no contact resistance, $\sigma_c = 0$. This yielded the expected results of no resulting current for probes 2 and 3 and a resulting current for probe 1 that was in good agreement with the analytically expected value for the resistance of one yarn, $R_1 = \frac{8 \text{ mm}}{10 \frac{\text{s}}{\text{mm}} \pi (0.15 \text{ mm})^2 10}$. The variation in the resulting currents for this static analysis is due to the strain being dependent entirely upon conduction through contacts. Using the constant isotropic conductivity constitutive law, the electrical resistances do not change because of the deformation due to the transformation of the conductivity tensor. The fibrils can be analyzed separately if they are insulated, allowing the electrical problem to always be pushed back into the reference configuration

$$I = \int_{\Gamma} \boldsymbol{\sigma} \nabla_x V \cdot \mathbf{n} \, d\Gamma, \quad (58)$$

$$= \int_{\Gamma_0} \left(\frac{1}{J} \mathbf{F} \boldsymbol{\sigma}_0 \mathbf{F}^T \right) (\mathbf{F}^{-T} \nabla_X V) \cdot J \mathbf{F}^{-T} \mathbf{N} \, d\Gamma_0, \quad (59)$$

$$= \int_{\Gamma_0} \boldsymbol{\sigma}_0 \nabla_X V \cdot \mathbf{N} \, d\Gamma_0. \quad (60)$$

Because the PDE is also solved in the reference configuration (Equation 8), all of these values are constant. Thus, the current passing through the boundary of each fibril would always be same

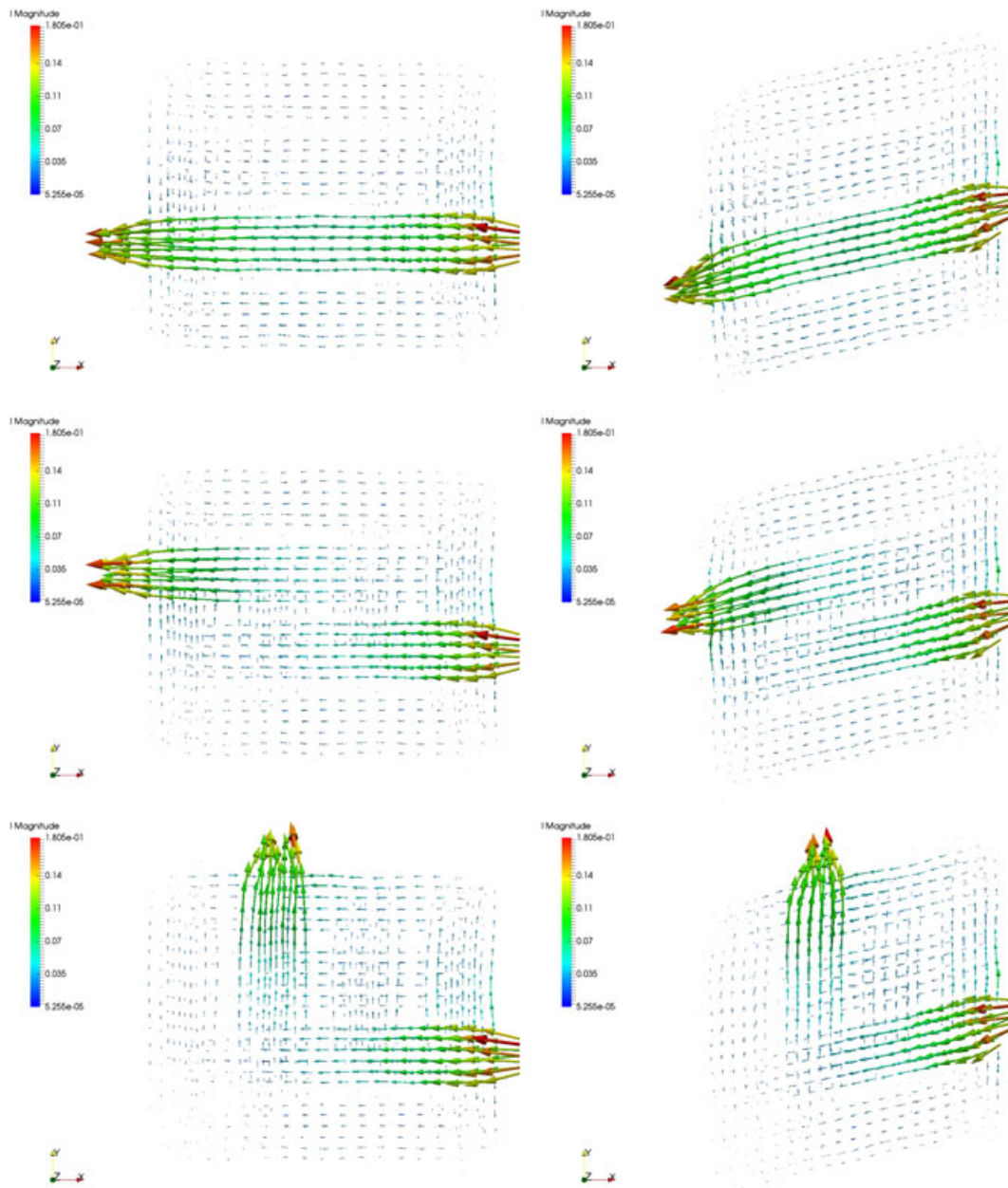


Figure 13. Current distributions for the three probe locations for the largest calculated strains for the stretching (left) and shearing (right). The current is the total through the cross section, measured in amps.

regardless of deformation—for the assumption of constant σ_0 . That is, the material deformation-induced texturing of the conductivity tensor does not effect the resistance of the body as long as the boundary conditions ‘follow the body’ and do not shift with respect to the reference state. It is possible to consider constitutive laws for the conductivity tensor that is dependent on the state of the material beyond the transformation from the reference configuration to current configuration, such as strain-dependent conductivity or plasticity. This would allow the resistance to change without the effect of contacts.

From the argument earlier regarding deformation of insulated conductors and the geometry of the yarns, it is expected that the resistance of a yarn segment is not a strong function of the contact forces (for more complicated yarns, such as heterogenous braided wires where contacts may play a strong roll inside a yarn, this may not be the case). This is the trend observed for both stretch cases

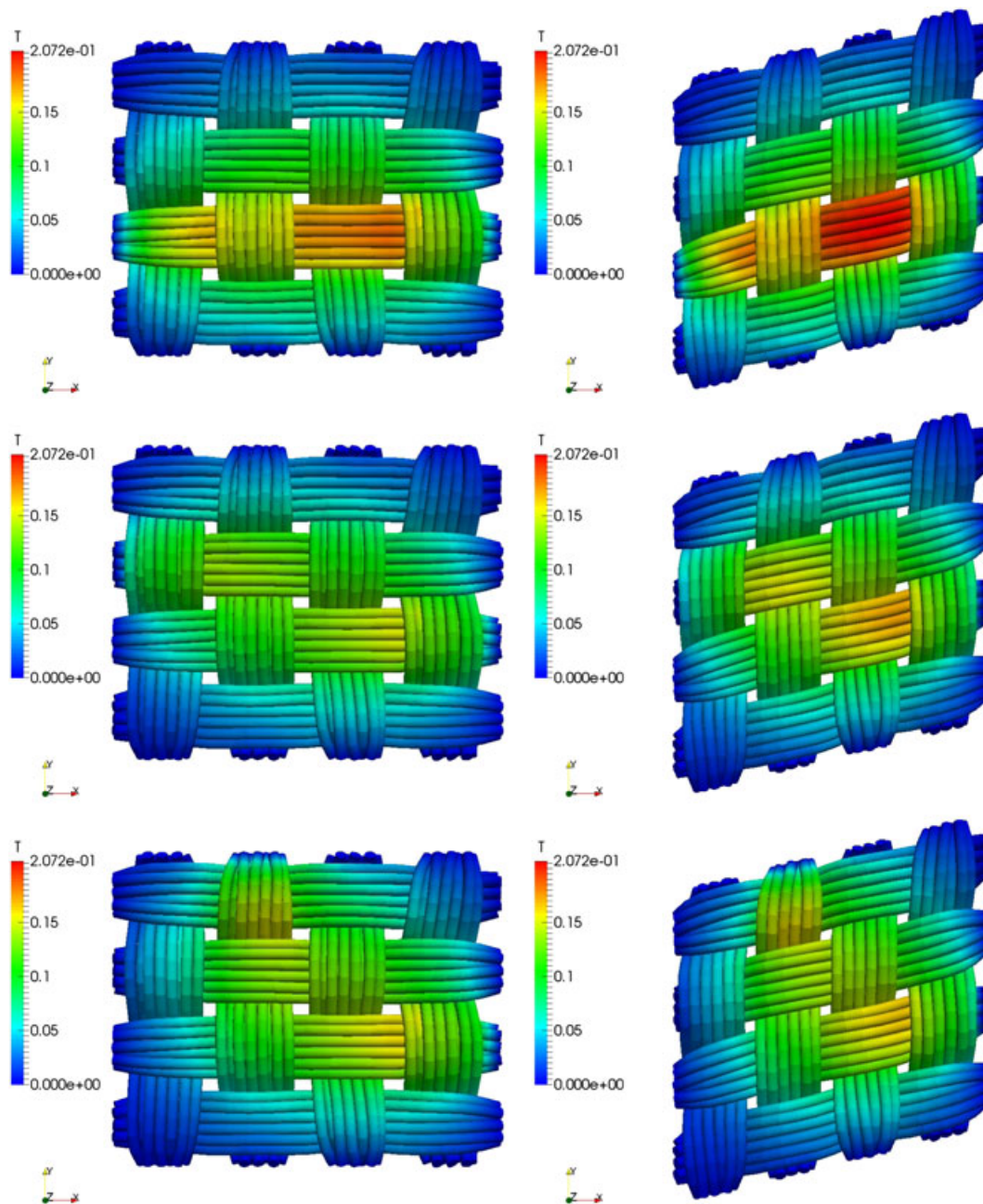


Figure 14. Temperature distributions due to Joule heating for the three probe locations for the largest calculated strains for the stretching (left) and shearing (right). The temperature is measured in degrees Celsius relative to the boundary.

in Figure 15. The variation can arise from both currents passing through contacts between fibrils in a yarn as the yarn bends, which alters the resistance slightly, and error in the fitting process to determine the best R_y . The error in the network model arises from the large area over which two yarns are in contact. A single node at the midpoint of each yarn segment is a good representation in the limit when the yarns become very slender so that their contact area is very small compared to their length. The plain woven fabric simulated is very dense, so the contact between two yarns takes place over most of their length. A better network model would add more contact resistors and nodes in parallel with smaller yarn segment resistors between them—but this defeats the purpose of an approximation.

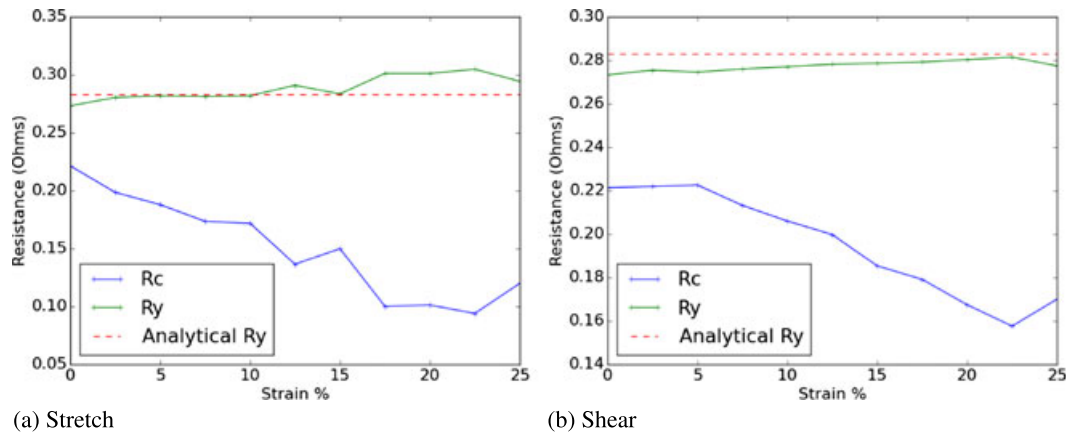


Figure 15. Resistor values as a function of stretch state, for the yarn segment, R_y (C), and the contact, R_c (C). (a) Stretch and (b) shear.

The contact resistance can change drastically as fibrils slide by each other. This causes the response current to change non-monotonically, and even reverse trend at some points. The resistance can be decreasing because of an increase in contact pressure between two fibrils, but as the deformation continues, a critical point can be passed in which the fibrils rearrange to a state with lower contact pressures, resulting in a higher resistance. As could be expected, the reaction current measured along a single yarn, probe 1, in Figure 12(e) and (f), is always the highest. However, the additional conducting paths present because of the electrical contacts allow the resistance to vary significantly as the textile deforms. The increase in contact pressures and the rearrangement of contacts cause the resistances for probes 2 and 3 to drop significantly on average as the textile is stretched in both cases.

9. CONCLUSION

A computational framework was developed for modeling textiles at the microstructure level using interwoven large deformation beams to represent individual fibrils. A contact model for beams was developed that incorporates the thermal and electrical resistances that scale with the contact force by approximating the contact area. An example was presented that predicts the mechanical, electrical, and thermal properties of a representative volume element of a simple plain woven fabric consisting of homogenous conducting fibrils. The simulation predicted the microstructure-dependent Poisson's ratio effect of the textile. The effective electrical resistance of the RVE was shown to depend on the strain state based on inter-fibril contact pressures and the slipping of fibrils. The simulation results were used to produce an effective contact resistance to model the conductive textile as a resistor Kirchhoff network.

The fibril configurations studied are not necessarily unique. Because of the discrete nature of the structures, other packings are possible, which will result in different local stresses that may affect the macroscopic response. A more detailed study would repeat the analyses on perturbed initial states to quantify the range of responses.

The level of discretization incorporated allows the representation of arbitrary microstructures, such as knitted textiles or heterogenous yarns. Current work on the model involves developing geometry generation schemes to produce the representative volume elements of more complicated fabrics that could be used in a design process. The framework developed is general enough to incorporate a wide variety of constitutive responses. A number of additions can be made to the constitutive laws to enable the study of different fabric materials and devices. Static friction has a significant effect on the energy dampening in the dynamic analysis as well as the effective shear strength of a textile in static analysis [51–53] and would thus be a significant improvement to the model. Pressure dependence conductivities can be used to improve the analysis of thermal and

electrical resistances in the textile. Piezoelectric and other electromagnetically coupled constitutive laws can be used to analyze textile-based electromechanical devices.

ACKNOWLEDGEMENTS

This work was funded by the Army Research Laboratory through the Army High Performance Computing Research Center (cooperative agreement W911NF-07-2-0027).

REFERENCES

1. Linz T, Simon E, Walter H. Fundamental analysis of embroidered contacts for electronics in textiles. *Electronic System-Integration Technology Conference (ESTC), 2010 3rd*: IEEE, Berlin, 2010; 1–5.
2. Post ER, Orth M, Russo PR, Gershenfeld N. E-broidery: design and fabrication of textile-based computing. *IBM Systems Journal* 2000; **39**(3.4):840–860.
3. Buechley L, Hendrix S, Eisenberg M. Paints, paper, and programs: first steps toward the computational sketchbook. *Proceedings of the 3rd International Conference on Tangible and Embedded Interaction*: ACM, 2009; 9–12.
4. Karaguzel B, Merritt CR, Kang T, Wilson JM, Nagle HT, Grant E, Pourdeyhimi B. Flexible, durable printed electrical circuits. *The Journal of the Textile Institute* 2009; **100**(1):1–9.
5. Cherenack K, Zysset C, Kinkeldei T, Münzenrieder N, Tröster G. Woven electronic fibers with sensing and display functions for smart textiles. *Advanced Materials* 2010; **22**(45):5178–5182.
6. Ghosh TK, Dhawan A, Muth JF. Formation of electrical circuits in textile structures. In *Intelligent Textiles and Clothing*, Mattila H (ed.). Woodhead Publishing: Cambridge, England, 2006; 239–282.
7. Krajewski A, Magniez K, Helmer R, Schrank V. Piezoelectric force response of novel 2D textile based PVDF sensors. *Sensors Journal, IEEE* 2013; **13**(12):4743–4748.
8. Vatansever D, Siores E, Hadimani RL, Shah T. Advances in modern woven fabrics technology. In *Chapter Smart Woven Fabrics in Renewable Energy Generation*, Vassiliadis S (ed.). INTECH Open Access Publisher, 2011; 252 pages. ISBN: 978-953-307-337-8.
9. Haines CS, Lima MD, Li N, Spinks GM, Foroughi J, Madden JDW, Kim SH, Fang S, de Andrade MJ, Göktepe F. *et al.* Artificial muscles from fishing line and sewing thread. *Science* 2014; **343**(6173):868–872.
10. Kuznetsov S, Fish J. Mathematical homogenization theory for electroactive continuum. *International Journal for Numerical Methods in Engineering* 2012; **91**(11):1199–1226.
11. Wentorf R, Collar R, Shephard MS, Fish J. Automated modeling for complex woven mesostructures. *Computer Methods in Applied Mechanics and Engineering* 1999; **172**(1):273–291.
12. Duan Y, Keefe M, Bogetti TA, Cheeseman BA, Powers B. A numerical investigation of the influence of friction on energy absorption by a high-strength fabric subjected to ballistic impact. *International Journal of Impact Engineering* 2006; **32**(8):1299–1312.
13. Gu B. Ballistic penetration of conically cylindrical steel projectile into plain-woven fabric target—a finite element simulation. *Journal of Composite Materials* 2004; **38**(22):2049–2074.
14. Chung PW, Tamma KK, Namburu RR. A micro/macro homogenization approach for viscoelastic creep analysis with dissipative correctors for heterogeneous woven-fabric layered media. *Composites Science and Technology* 2000; **60**(12):2233–2253.
15. Nadler B, Papadopoulos P, Steigmann DJ. Multiscale constitutive modeling and numerical simulation of fabric material. *International Journal of Solids and Structures* 2006; **43**(2):206–221.
16. Fillep S, Mergheim J, Steinmann P. Computational homogenization of rope-like technical textiles. *Computational Mechanics* 2015; **55**(3):577–590.
17. Tan VBC, Ching TW. Computational simulation of fabric armour subjected to ballistic impacts. *International Journal of Impact Engineering* 2006; **32**(11):1737–1751.
18. Leech CM, Adeyefa BA. Dynamics of cloth subject to ballistic impact velocities. *Computers & Structures* 1982; **15**(4):423–432.
19. Zohdi TI, Powell D. Multiscale construction and large-scale simulation of structural fabric undergoing ballistic impact. *Computer Methods in Applied Mechanics and Engineering* 2006; **195**(1-3):94–109.
20. Zohdi TI. High-speed impact of electromagnetically sensitive fabric and induced projectile spin. *Computational Mechanics* 2010; **46**(3):399–415.
21. Zohdi TI. Electromagnetically-induced deformation of functionalized fabric. *Journal of Elasticity* 2011; **105**(1): 381–398.
22. Beex LAA. Multiscale quasicontinuum modelling of fibrous materials. *Ph.D. Thesis*, 2012.
23. Wang Y, Sun X. Digital-element simulation of textile processes. *Composites Science and Technology* 2001; **61**(2):311–319.
24. Zhou G, Sun X, Wang Y. Multi-chain digital element analysis in textile mechanics. *Composites Science and Technology* 2004; **64**(2):239–244.
25. Miao Y, Zhou E, Wang Y, Cheeseman BA. Mechanics of textile composites: micro-geometry. *Composites Science and Technology* 2008; **68**(7):1671–1678.

26. Zhou E, Mollenhauer DH, Larve EV. A realistic 3-D textile geometric model. *Seventeenth International Conference on Composite Materials ICCM-17*, Edinburgh, United Kingdom, 2009.
27. Wang Y, Miao Y, Swenson D, Cheeseman BA, Yen C-F, LaMattina B. Digital element approach for simulating impact and penetration of textiles. *International Journal of Impact Engineering* 2010; **37**(5):552–560.
28. Durville D. Modelling of contact–friction interactions in entangled fibrous materials. *Vi World Wide Congress on Computational Mechanics*, Beijing, China, 2004.
29. Durville D. Finite element simulation of textile materials at mesoscopic scale. *Finite Element Modelling of Textiles and Textile Composites*, 2007.
30. Durville D. A finite element approach of the behaviour of woven materials at microscopic scale. In *Mechanics of Microstructured Solids*, Vol. 46. Lecture Notes in Applied and Computational Mechanics: Springer, 2009; 39–46.
31. Laurent CP, Durville D, Mainard D, Ganghoffer J-F, Rahouadj R. A multilayer braided scaffold for anterior cruciate ligament: mechanical modeling at the fiber scale. *Journal of the Mechanical Behavior of Biomedical Materials* 2012; **12**:184–196.
32. Durville D. Contact–friction modeling within elastic beam assemblies: an application to knot tightening. *Computational Mechanics* 2012:1–21.
33. Bajas H, Durville D, Ciazynski D, Devred A. Numerical simulation of the mechanical behavior of ITER cable-in-conduit conductors. *Applied Superconductivity, IEEE Transactions on* 2010; **20**(3):1467–1470.
34. Torre A, Bajas H, Ciazynski D, Durville D, Weiss K. Mechanical-electrical modeling of stretching experiment on 45 strands CICC. *Applied Superconductivity, IEEE Transactions on* 2011; **21**(3):2042–2045.
35. Logg A, Mardal K-A, Wells G. *Automated Solution of Differential Equations by the Finite Element Method: The Fenics Book*, Vol. 84. Springer Science & Business Media: Berlin, 2012.
36. Kovetz A. *Electromagnetic Theory*. Oxford University Press: Oxford, 2000.
37. Steigmann DJ. On the formulation of balance laws for electromagnetic continua. *Mathematics and Mechanics of Solids* 2007.
38. Rubin MB. *Cosserat Theories: Shells, Rods and Points*, Solid Mechanics and its Applications, vol. 79. Kluwer Academic Publishers: Dordrecht, 2000.
39. Incropera FP, Frank PI, David PD, Theodore LB, Adrienne SL. *Fundamentals of Heat and Mass Transfer* (6th edition). John Wiley & Sons: Hoboken, NJ, 2011.
40. Johnson KL. *Contact Mechanics*. Cambridge University Press: Cambridge, 1987.
41. Tao X. Electrical textile sensors for repeated large deformation: structures and electromechanical properties. *International Conference on Experimental Mechanics 2008 and Seventh Asian Conference on Experimental Mechanics*: International Society for Optics and Photonics, Nanjing, China, 2008; 73754H–73754H.
42. Haseganu EM, Steigmann DJ. Analysis of partly wrinkled membranes by the method of dynamic relaxation. *Computational Mechanics* 1994; **14**(6):596–614.
43. Logg A, Wells GN, Hake J. Dofin: a c++/Python finite element library. In *Lecture Notes in Computational Science and Engineering*. Springer: Berlin Heidelberg, 2012; 173–225.
44. Logg Anders. *et al.* “Ffc: the fenics form compiler.” In *Automated Solution of Differential Equations by the Finite Element Method*. Springer: Berlin Heidelberg, 2012; 227–238.
45. Queiruga AF. Microscale simulation of the mechanical and electromagnetic behavior of textiles. *Ph.D. Thesis*, 2015.
46. Van Der Walt S, Colbert SC, Varoquaux G. The NumPy array: a structure for efficient numerical computation. *Computing in Science & Engineering* 2011; **13**(2):22–30.
47. Jones E, Oliphant T, Peterson P, *et al.* SciPy: open source scientific tools for Python, 2001. (Available from: <http://www.scipy.org/>) [Online; accessed 2016-01-01].
48. Wolfram Research Inc. *Mathematica*. Wolfram Research, Inc.: Champaign, Illinois, Version 9.0 edition, 2012.
49. Hunter JD. Matplotlib: a 2D graphics environment. *Computing in Science and Engineering* 2007; **9**(3):90–95.
50. Henderson A, Ahrens J, Law C, *et al.* *The Paraview Guide*. Kitware Clifton Park: NY, 2004.
51. Briscoe BJ, Motamedi F. The ballistic impact characteristics of aramid fabrics: the influence of interface friction. *Wear* 1992; **158**(1):229–247.
52. Kirkwood JE, Kirkwood KM, Lee YS, Egres RG, Wagner NJ, Wetzel ED. *et al.* Yarn pull-out as a mechanism for dissipating ballistic impact energy in kevlar® km-2 fabric part ii: predicting ballistic performance. *Textile Research Journal* 2004; **74**(11):939–948.
53. Kirkwood KM, Kirkwood JE, Lee YS, Egres RG, Wagner NJ, Wetzel ED. *et al.* Yarn pull-out as a mechanism for dissipating ballistic impact energy in kevlar® km-2 fabric part i: quasi-static characterization of yarn pull-out. *Textile Research Journal* 2004; **74**(10):920–928.